Charge exchange imaging of space plasmas (invited)

Earl Scime[a] and Anna Zaniewski
Department of Physics, West Virginia University, Morgantown, West Virginia 26506-6315

(Presented on 19 April 2004; published 5 October 2004)

Detection of neutral atom emission from hot plasmas has evolved to the point where it is now possible to image hot plasmas in neutral atom emission. In this work, we review a variety of successful approaches to space-based neutral atom imaging and discuss the qualitative and quantitative information that can be obtained from neutral atom images, e.g., hot ion transport and ion temperatures. A challenging aspect of neutral atom imaging of the Earth's magnetosphere is that the combination of small neutral fluxes and spacecraft motion necessitates the development of algorithms capable of summing neutral emission obtained from different vantage points over many months to obtain statistically significant images. The image summing algorithm and typical summed images are also presented in this work. © *2004 American Institute of Physics* .
[DOI: 10.1063/1.1779618]

I. NEUTRAL ATOM EMISSION IMAGE ANALYSIS

After Roelof demonstrated that energetic particle measurements inadvertently obtained during cusp transits by the IMP 7/8 and ISEE-1 spacecraft were consistent with the detection of energetic neutral atoms[1] and that neutral atom emission could be used to create neutral atom images,[2] the space plasma community embraced the concept of neutral atom imaging. Remote neutral atom imaging of the magnetosphere is based on the detection and imaging of energetic neutral atoms created in the magnetosphere through charge exchange collisions. The Earth's magnetospheric plasma coexists with the diffuse, very low temperature, neutral atom atmosphere (the geocorona) that surrounds the Earth.[3,4] In regions where the geocorona coexists with hot plasma, fast ions undergo charge exchange collisions with the background neutral atoms; producing a cold ion and a neutral atom with the same energy as the original ion. The cross section for charge exchange collisions between ions and neutrals is a strong function of center of mass energy and is well known from laboratory measurements.[5] In laboratory plasma experiments, where neutral atom measurements were first employed,[6] this type of neutral atom measurement is called a charge exchange measurement. The typically peaked ion temperature profiles of laboratory plasmas yield a neutral atom energy spectrum from which the ion temperature is easily extracted if the plasma is optically thin.[7]

Since 1987, a variety of methods for neutral atom imaging have been considered in the scientific literature and instruments based on some of the proposed techniques have flown in space. Gruntman's review of the history of space-based neutral atom detection, neutral atom imaging, and the different techniques that can be used to image neutral atoms is an excellent resource for readers interested in an in-depth discussion of neutral atom imaging.[8] Only a brief review of the essential elements of neutral atom imaging methods is presented here for the reader who is unfamiliar with the principal advantages and limitations of the different approaches to neutral atom imaging. One of the early approaches to neutral atom imaging involved the coupling of charge conversion elements to conventional, trajectory resolving, ion spectrometers.[8,9] As shown in Fig. 1(a), a charge conversion foil strips incoming neutrals into ions which are then resolved in energy and incident angle by the analyzer. Because the flux of background Ultraviolet (UV) photons can be 10^6–10^8 times larger than the neutral flux,[10] the removal of the newly created ions from the photon path through the imager is essential in reducing the background signal to manageable levels. The principal drawbacks to this approach are the poor conversion efficiency of the foil (as much as 90% of the neutrals pass through the foil without charge conversion) and that to increase the geometric factor of the instrument (the total count rate) the volume of the electrostatic analyzer must increase. Since mass and volume are both limited on spacecraft, this approach is problematic. The combination of stripping foil and electrostatic analyzer is often used to obtain single line of sight, neutral atom emission measurements from hot laboratory plasmas where mass and volume are not so constrained.[11]

A much more compact, larger geometric factor, direct-detection, neutral atom imager was developed for the Cassini spacecraft (launched in 1997 and expected to arrive at Saturn in July of 2004). In the ion neutral camera (INCA) instrument, energetic neutrals pass through a set of collimating plates, then they pass through a carbon foil covered slit and strike a position and energy resolving solid state detector.[12,13] The carbon foil is thick enough to block the UV and the combination of the slit and the position sensitive detector provide determination of the incident neutral trajectory [see Fig. 1(b)]. Spacecraft spin sweeps the collimated view of the INCA instrument through 360° and the result is a two dinunrional (2D) image of energy resolved neutral atom flux. Secondary electrons generated on the backside of the carbon foil by the passage of the neutral atoms provide a timing start

[a]Electronic mail: escime@wvu.edu

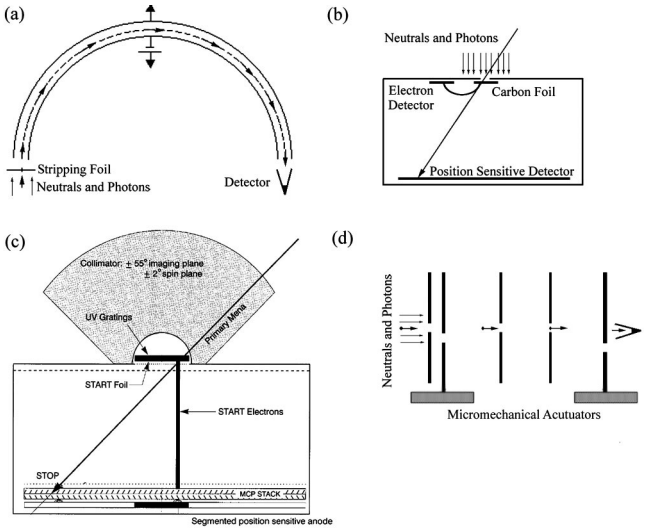

FIG. 1. (a) Neutral detection based on charge conversion followed by electrostatic analysis. (b) Essential elements of the INCA imager: slit camera; position sensitive, energy resolving detector; thick carbon foil for UV blocking and start timing pulse; and electron detector for time-of-flight measurement. (See Ref. 13) (c) Essential elements of the MENA imager: high voltage collimators for charged particle rejection; UV blocking grating; start pulse carbon foil; and position sensitive detector for neutrals and electrons. (See Ref. 20.) (d) Schematic of a hypothetical neutral detector based on mechanical shutters moved by micromechanical actuators or resonantly oscillating piezoelectric crystals. (See Ref. 9.) Such a detector does not place an intrinsic lower limit on the neutral energy.

pulse for coincidence detection (to reduce background counts) and for time-of-flight measurements that, when combined with the neutral energy measurements, yield the mass of the incident neutral. The limiting feature of the INCA instrument is the threshold energy required for penetration of the carbon foil by the neutral atoms. To transit the carbon foil without significant energy loss or angular scattering, neutral hydrogen energies of more than 50 keV are required.

Since much of the inner magnetospheric and plasmasheet neutral atom emission occurs at energies less than 20 keV,[14–16] direct detection methods that did not require UV blocking foils,[10] first suggested by Gruntman in 1991, were also investigated by a number of research groups. In Gruntman's original concept, neutral atoms fell directly onto a position sensitive detector while photons were eliminated by a filtering structure that permitted the passage of atoms but not ultraviolet photons [Figure 1(c)]. Free-standing gold gratings with nominal 150 nm bars and 50 nm gaps have roughly 10^{-6} UV transmissions and 10^{-1} atom transmissions;[17,18] ideal for use as UV blockers in a direct detection neutral atom imager. The medium energy neutral atom (MENA) imager launched aboard the IMAGE spacecraft[19] in 2000 is a grating-based, direct detection neutral atom imager.[20] MENA is composed of three sensor heads, each of which functions as an independent wide slit camera. Each head provides a one-dimensional image of incident ENAs; the second imaging direction is obtained from the spacecraft spin. As neutral atoms transverse through the instrument, they enter through a charged particle deflecting collimator. The neutral atoms then pass through a UV blocking grating and the fraction that pass through the grating then transit a thin carbon foil. The passage of a neutral atom through the carbon foil typically liberates one or more secondary electrons. The electrons are then accelerated to the microchannel plate detector Start segment. When the atom arrives in the Stop segment of the detector, the incident angle and time-of-flight (TOF) are determined using the corresponding Start and Stop data. The trajectory and TOF measurements are then combined to calculate the neutral atom speed.[20,21] A coincidence requirement for valid events reduces background from light and penetrating radiation. On a statistical basis, the fraction of different ENA species can, in principle, be determined from detector pulse heights, but such measurements are not routinely made. On-board the spacecraft, TOF, start and stop positions are processed into energy-resolved images and telemetered to the ground (called "on-board data"), along with direct-event data (called "statistics data"). The on-board data is processed using an approximate calibration algorithm and returns limited energy resolution images. Specifically, the on-board data is binned into only five energy levels. For energy spectra analyses, such as ion temperature measurements, the better energy resolution of the statistics data is preferable. However, the statistics data is limited by the number of events that can be reported per spacecraft spin, substantially reducing the total counts reported during periods of intense geomagnetic activity (corresponding to large neutral fluxes). Since the limitation is on the number of events counted per 8° of azimuthal spin, the azimuthal resolution of the statistics data is often limited to 8° during intervals of intense geomagnetic activity. A separate measure of the total number of events counted per spacecraft spin enables scaling of the statistics event rate data to the more complete on-board count rate data.

The entire MENA instrument, including power supplies, masses 13.2 kG and consumes 22.5 W of power. The azimuthal, "spin," angular coverage of the instrument is 360° with 4° resolution determined by the angular acceptance of the collimating structure. The polar, "imaging," coverage spans 160° with a typical imaging resolution of 4°. Each individual head has a polar imaging range of only 120°, but each head is offset by 20° to compensate for the 20° blind spot in the center of each head (due to an inability to distinguish between electrons and neutrals striking the electron detection region of the imaging microchannel plate stack). The microchannel plate detector consists of a custom z stack of Hamamatsu microchannel plates (MCPs) in front of a position sensitive anode. The MCPs provide large area (72 mm$\times$90 mm), relatively high resistance ($\sim$100 M Ω per plate), high gain due to channels with 60:1 length-to-diameter ratio, and narrow pulse height distribution (as low as 70% over the entire detector). The MCPs also operate with low noise (<1 cm^{-2} s^{-1}), very low rate of after-pulsing as required for the TOF work, and excellent uniformity ($<$10% variations over their surface). The 1–70 keV/nucleon energy range and geometric factor of 0.1 cm^2 sr of MENA is adequate to detect ENA's from the inner magnetosphere, ring current, and plasma sheet.

Even the thin, 40 Å thick, foils used in the MENA instrument limit detection to neutrals with energies greater than 1 keV. Therefore, sophisticated indirect detection schemes relying on contact ionization of neutrals have been devel-

oped (and flown on the IMAGE mission) to image neutrals in the energy range of a few eV to a few hundreds of eV.[22] Direct detection schemes without intrinsic energy range limitations, such as mechanical choppers[23] or the vibrating shutter technique shown in Fig. 1(d), have been proposed for future neutral atom imaging missions.[9] However, flight worthy micromechanical structures needed to implement such imaging techniques in a compact, lightweight instrument are still under development.[24]

II. NEUTRAL ATOM EMISSION IMAGE ANALYSIS

Raw energetic neutral atom flux images, flux versus spin and imaging angle, are obtained from the three neutral atom imagers[20,25,26] aboard the IMAGE spacecraft every 2 min (every spin). The raw time and energy resolved images are used to qualitatively investigate dynamic magnetospheric processes such as plasma injections during large geomagnetic storms[14] and the dramatic increase in plasmasheet density that accompanies large storms.[27] The details of the energy spectra of the neutral flux, as well as the transport of ions in the inner magnetosphere, are now routinely used to determine magnetospheric electric fields[28] and in conjunction with sophisticated models, can be used to determine the pitch angle distribution of ions in the equatorial plane.[29] However, even without inverse modeling techniques, quantitative information, specifically ion temperatures, can be extracted from neutral atom images.

For energetic neutral atom emission along a given viewing direction, the contribution to the high-energy portion of the energy spectrum (energies much greater than the ion temperature) from a hot space plasma is dominated by emission from the hottest region along the line of sight. The high-energy portion of the neutral atom energy spectrum, $F(E)$, generated via charge exchange collisions for a Maxwellian ion distribution of temperature T, is given by[7]

$$F(E)dE \approx C\sigma(E)E\ dE\left(\frac{n_o(r)n_i(r)e^{\frac{-E}{T(r)}}}{\sqrt{2m_i\pi^3T(r)^3}}\right)_{r=x} \times \exp - \int_x^a \alpha(l)dl, \quad (1)$$

$F(E)$ is in units of $\#/\mathrm{cm}^2$ s, C is a constant that accounts for the geometrical viewing properties of the instrument and the column line-of-sight integration over the hottest region (located at some point x along the line of sight). The hottest region is assumed to be of constant temperature and therefore the column integration of the neutral emission region yields a constant multiplicative factor. $T(x)$, $n_o(x)$, and $n_1(x)$ are the ion temperature, neutral density, and ion density at the same location, respectively. $\sigma(E)$ is the energy dependent charge exchange cross section[5] between neutrals and ions of energy E and the integral over $\alpha(l)$ accounts for the reduction of neutral flux originating from the location of the hottest region due to additional collisions or ionization as the neutrals travel from point x to the instrument located at point a. Outside of the plasmapause, the ion[30] and neutral densities[4] are low enough that the magnetosphere is optically thin to energetic neutral atom emission. Thus,

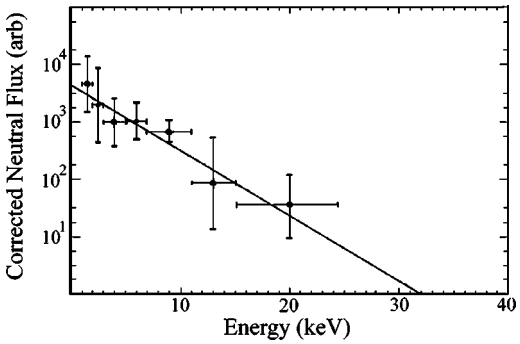

FIG. 2. Logarithm of the corrected neutral atom flux versus neutral energy and a fit to the data using Eq. (2).

$$\frac{F(E)dE}{\sigma(E)E\ dE} \approx C\left(\frac{n_o(x)n_i(x)}{\sqrt{2m_i\pi^3T(x)^3}}\right)e^{\frac{-E}{T(x)}}. \quad (2)$$

This analysis assumes the neutral atom fluxes are due to charge exchange between protons and neutral hydrogen. The energy bins of the MENA instrument are based solely on TOF measurements, and thus the mass (and energy) of the neutral atoms is not known.

A standard least squares linear fit with Eq. (2) is used to determine the peak ion temperature along the line of sight for statistics data sorted into seven energy bins and corrected for the energy-dependent charge exchange cross section. An example spectrum is shown in Fig. 2 for a single imaging line-of-sight (imaging pixel). Although the MENA instrument is capable of measuring neutral energies of up to 70 keV/nucleon, energies above 25 keV were excluded from the analysis presented here to avoid complications arising from background counts and known instrumental artifacts. The statistical error in each ion temperature determination is calculated based on the uncertainties in the energies of each energy bin and on the statistical uncertainty in the number of counts in each energy bin.

During storm times, the remotely determined ion temperatures in a single imaging pixel are consistent in both magnitude and temporal evolution with in-situ ion temperatures obtained by spacecraft located the imaging line-of-sight corresponding to that pixel (see Fig. 3 for a comparison of MENA and *in situ* MPA [31] data).[32] During magnetospherically quiet intervals, the neutral fluxes are too small to extract either qualitative or quantitative information from the images. To improve the precision of the ion temperature measurements, either the individual temperature measurements or the raw neutral fluxes (followed by temperature analysis) can be averaged over time. Averaging the raw fluxes over 1 h intervals is sufficient to obtain statistically significant ion temperature measurements for geomagnetically active intervals and longer integrations are required for geomagnetically quiet intervals.[33] Because the IMAGE spacecraft is in a highly elliptical orbit and MENA image pixels are typically $4° \times 4°$, significant blurring of small scale structures due to the motion of the spacecraft can occur on 1 h time scales. In addition, the location of the Sun-Earth line moves in the MENA image plane throughout the IMAGE mission due to the precession of the line of apsides and motion of the Earth around the Sun, i.e., the

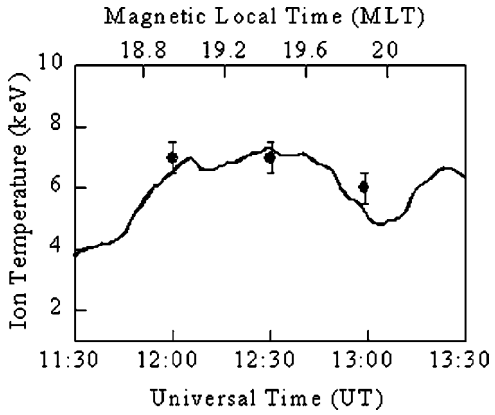

FIG. 3. Ion temperature versus time obtained from the 1994-84 Magnetospheric Plasma Analyzer instrument (solid line) in geosynchronous orbit and in the field of view of the MENA instrument. (See Ref. 32.) Data have been smoothed with a 20 min boxcar average for consistency with the MENA image data. Remotely measured ion temperatures from MENA data (solid circles) with ±0.5 eV error bars at 12:00, 12:30, and 13:00 UT.

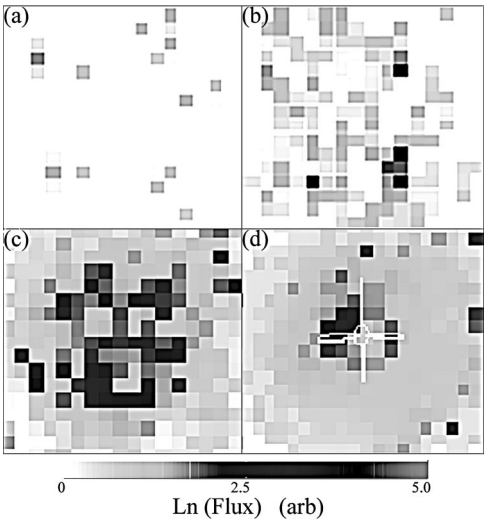

FIG. 4. Quiet time ($D_{st} \sim 0$) magnetospheric 1–2 keV neutral atom flux (a) for a single 2 min acqusition, (b) averaged ten images, (c) averaged over 80 images, and (d) for 27–60 keV neutral atom flux averaged over 1028 images.

viewing geometry changes significantly because of seasonal changes and orbital precession. Therefore, an imaging summing algorithm was developed to correct for spacecraft motion and to permit the addition of images from different orbits throughout the entire mission.

To average images over intervals longer than 1 h, we project each line of sight to a $1R_E \times 1R_E$ fixed grid placed in the equatorial plane. The neutral fluxes measured along each line of sight are then binned according to which grid sector the line of sight intersects.[33] To account for the different lengths of time that each grid sector in view, the total flux in each grid sector was then normalized by the number of times that particular grid sector was viewed by the MENA instrument. Similar mapping techniques have been used previously for ENA image data from the Polar spacecraft.[34] However, here the data are mapped to the same fixed grid regardless of the season of the orbit or the location of the spacecraft. The fluxes have been projected to the equatorial plane and aligned so that the Sun is to the right and the Earth in the center in each image. $L=2$ and $L=4$ representative magnetic field lines are shown centered on the Earth. The ring current, with a typical scale size of a single pixel and a pre-midnight enhancement, is clearly evident in Fig. 4(d).

The image sequence shown in Fig. 4 demonstrates the improvement in the signal-to-noise of neutral atom images obtained as our flux mapping algorithm is applied to larger and larger sets of images acquired during intervals of negligible geomagnetic activity (disturbance storm time index, $D_{st} \sim 0$). A single 2 min integrated image is shown in Fig. 4(a). An average over ten images is shown in Figure 4(b) and an 80 image average ($\sim$2.5 h) is shown in Figure 4(c). In the 80 image average, the neutral flux is clearly most intense in the center of the image (around the Earth) and discrete structures are visible. An averaged image based on 1028 individual images, over 34 h of data, is shown in Fig. 4(d). In all of the images in Fig. 4, the Sun is to the right, the Earth is in the center of the image, and the view is from above the magnetic north pole, i.e., the image data is mapped according to magnetic local time (MLT).

A well defined, quiet time ring current is visible in the 1028 image average between 2 and 4 R_E in this equatorial projection. The ring current is 1 grid element in size (1 R_E) centered on 3 R_E with a discrete, macroscopic feature in the pre-midnight sector. In situ measurements indicate that the quiet time ring current consists primarily of protons, is located between 2 and 5 R_E, and has a peak ion flux between 50 and 100 keV.[35] This long term average image of MENA data is the first ever global view of the of the quiet time inner magnetosphere. Because the images used in Fig. 4(d) were obtained from intervals evenly distributed around the Earth's orbit around the Sun, there is no bias in the average image due to seasonal effects or viewing geometry.

III. SUPERIMPOSED EPOCH ANALYSIS OF A GEOMAGNETIC STORM

To obtain reliable ion temperature images with sufficient time resolution to investigate the temporal evolution of a large geomagnetic disturbance, images from well defined stages of many storms can be averaged together. During a geomagnetic storm, material from the plasma sheet is driven into the near-Earth magnetosphere, enhancing the ring current. Since the majority of neutral atoms detected by the MENA instrument originate in the ring current D_{st}, which essentially measures the strength of the ring current, is an appropriate index by which to quantify storm strength and phase as it relates to neutral atom emission.[36,37] The evolution of the remotely measured ion temperatures averaged over 30 storms between May 2000 and March 2002 is shown in Fig. 5. Each storm had a minimum D_{st} of at least -50 and the storms were divided into phases based on their D_{st} profile: prestorm, main, early recovery, and late recovery.[33] The prestorm phase is relatively featureless in MLT, with ion temperatures of 2–3 keV throughout the inner magnetosphere. During the main phase, the magnetosphere generally heats up to temperatures of about 7 keV and the slightly hotter ring current is visible around $5-6R_E$. During the early

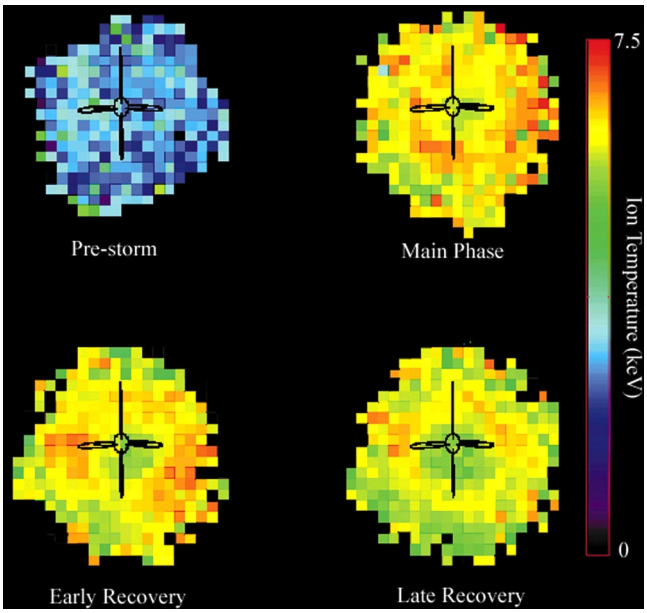

FIG. 5. (Color online) Prestorm, main phase, early recovery, and late recovery ion temperature images averaged over 30 different storms.

recovery and late recovery phases, the ion temperature in the dawn region is slightly lower then in the noon, dusk, and midnight sectors of the ring current. During late recovery, the bulk of the magnetosphere cools to around 5 keV, consistent with a loss of energetic ions through charge exchange, Coulomb interactions or other loss processes.

IV. DISCUSSION

These results demonstrate that magnetospheric ion temperatures can be remotely determined through charge exchange analysis. Through long term averaging, even the quiet time magnetosphere can be imaged in neutral atoms. Combining a superimposed epoch analysis of many storms with a new image summing algorithm enables the construction of time and spatially resolved ion temperature images of the terrestrial magnetosphere. Already new neutral atom imaging missions are under consideration by NASA. Researchers have suggested that these new missions might be capable of imaging the heliospheric termination shock[38] or perhaps even energetic neutral atoms created at the leading edge of coronal mass ejections headed towards the Earth.[39]

ACKNOWLEDGMENTS

The MENA instrument principal investigator is Craig Pollock of Southwest Research Institute. Design and construction of the instrument also involved researchers from the Japanese Institute of Space and Astronautical Sciences, Los Alamos National Laboratory, Goddard Space Flight Center, Rutherford Appleton Laboratory, University of Southern California, University of California at Berkeley, MIT, Auburn University, and Philips Research Laboratories. This work was supported at WVU under NASA Contract No. NAS5-96020

[1] E. C. Roelof, D. Mitchell, and D. Williams, J. Geophys. Res. **90**, 10991 (1985).
[2] E. C. Roelof, Geophys. Res. Lett. **14**, 652 (1987).
[3] N. Ostgaard *et al.* J. Geophys. Res., [Atmos.] (in press, 2003).
[4] R. L. Rairden, L. A. Frank, and J. D. Craven, J. Geophys. Res. **91**, 13613 (1986).
[5] R. L. Freeman and E. M. Jones, Atomic Collision Processes in Plasma Physics Experiments, Culham Laboratory Report No. CLM-R, 1974, p. 131.
[6] V. V. Afrosimov *et al.*, Sov. Phys. Tech. Phys. **20**, 33 (1975).
[7] I. H. Hutchinson, *Principles of Plasma Diagnostics* (Cambridge University Press, Cambridge, 1987).
[8] M. Gruntman, Rev. Sci. Instrum. **68**, 3617 (1997).
[9] H. O. Funsten *et al.*, J. Spacecr. Rockets **32**, 899 (1995).
[10] M. A. Gruntman, Proc. SPIE **1549**, 385 (1991).
[11] W. A. de Zeeuw *et al.*, Rev. Sci. Instrum. **62**, 110 (1991).
[12] D. G. Mitchell *et al.*, Opt. Eng. (Bellingham) **32**, 3096 (1993).
[13] D. G. Mitchell *et al.*, Space Sci. Rev. **91**, 67 (2000).
[14] C. J. Pollock *et al.*, Geophys. Res. Lett. **28**, 1147 (2001).
[15] D. T. Young, Rev. Geophys. Space Phys. **21**, 402 (1983).
[16] K. R. Moore *et al.*, Opt. Eng. (Bellingham) **33**, 342 (1994).
[17] E. E. Scime *et al.*, Appl. Opt. **34**, 648 (1995).
[18] M. M. Balkey *et al.*, Appl. Opt. **37**, 5087 (1998).
[19] J. L. Burch, Space Sci. Rev. **91**, 1 (2000).
[20] C. J. Pollock *et al.*, Space Sci. Rev. **91**, 113 (2000).
[21] M. G. Henderson *et al.*, J. Geophys. Res. (submitted).
[22] T. E. Moore *et al.*, Space Sci. Rev. **91**, 155 (2000).
[23] J. H. Moore, Jr. and C. B. Opal, Space Sci. Instrum. **1**, 377 (1975).
[24] D. J. McComas *et al.*, Rev. Sci. Instrum. **74**, 3874 (2003).
[25] D. G. Mitchell *et al.*, Space Sci. Rev. **91**, 67 (2000).
[26] T. E. Moore, Geophys. Res. Lett. **28**, 1143 (2001).
[27] D. J. McComas *et al.*, Geophys. Res. Lett. **29**, 36 (2002).
[28] P. C. Brandt *et al.*, Geophys. Res. Lett. **29**, 15 (2002).
[29] J. D. Perez *et al.*, Geophys. Res. Lett. **28**, 1155 (2001).
[30] M. Kivelson and C. T. Russell, *Introduction to Space Physics* (Cambridge University Press, New York, 1995).
[31] S. J. Bame *et al.*, Rev. Sci. Instrum. **64**, 1026 (1993).
[32] E. E. Scime *et al.*, Geophys. Res. Lett. **29**, 10.1029/2001GL013994 (2002).
[33] A. M. Zaniewski *et al.*, J. Geophys. Res. (submitted).
[34] G. D. Reeves and M. G. Henderson, J. Geophys. Res. **106**, 5833 (2001).
[35] I. A. Daglis *et al.*, Rev. Geophys. **37**, 407 (1999).
[36] Y. Ebihara *et al.*, Geophys. Res. Lett. **26**, 2929 (1999).
[37] A. M. Jorgensen *et al.*, Geophys. Res. Lett. **24**, 3173 (1997).
[38] M Gruntman *et al.*, J. Geophys. Res. **106**, 15767 (2001).
[39] M. Gruntman, J. Geophys. Res. **99**, 19213 (1994).